nature climate change

SUPPLEMENTARY INFORMATION

DOI: 10.1038/NCLIMATE1683

Geophysical limits to global wind power

Kate Marvel
Program for Climate Model Diagnosis and Intercomparison
Lawrence Livermore National Laboratory
P.O. Box 808, L-103
Livermore, CA 94551 USA
marvel1@llnl.gov

Ben Kravitz
Carnegie Institution
Department of Global Ecology
260 Panama Street
Stanford, CA 94305 USA
bkravitz@dge.stanford.edu

Ken Caldeira
Carnegie Institution
Department of Global Ecology
260 Panama Street
Stanford, CA 94305 USA
kcaldeira@dge.stanford.edu

August 17, 2012

A Supporting Online Material

A.1 Drag Parametrization

In this section, we discuss the parameter ρ_{Area} used to represent the large-scale effects of additional momentum sinks. This parameter, which has units of inverse length, represents the effective area covered by drag per square meter of atmosphere. $\rho_{Area} = 10^{-9}$ therefore corresponds to one square meter of extraction area per cubic kilometer of atmosphere, while the largest value used here, $\rho_{Area} = 10^{-5}$, corresponds to 10,000 square meters of extraction area per cubic kilometer. An increase in ρ_{Area} therefore corresponds to an increase in effective drag. Alternatively, this term can be thought of as the inverse of a kinetic energy extraction length scale L: the mean distance a parcel of air moves before losing its momentum to added momentum sinks (i.e., additional drag). Thus, when $\rho_{Area} = 10^{-9}$, the average parcel of air travels one million kilometers before losing its momentum to the additional sinks, and when $\rho_{Area} = 10^{-5}$, a parcel of air may travel only 100 km before losing momentum.

This means that the effect of additional drag may also be parameterized in terms of a timescale for kinetic energy extraction. This is, equivalently, the timescale for energy to be transported to effective drag areas. This time scale varies in space and time and is inversely proportional to local wind speed. Figure A1(d) shows the quotient of the global total kinetic energy extraction rate and the global total atmospheric kinetic energy for each of our simulations. In the SL simulations, this timescale ranges from almost 200 years in the SL(9) case to 20 days in the SL(5) cases. In the WA simulations, the timescale ranges from one year to about 5 hours. Figure A1(e), by contrast, show the kinetic energy *residence* time, defined as the quotient of the total dissipation rate and the total kinetic energy.

These momentum sinks reduce the kinetic energy of the atmosphere through two basic mechanisms. First, as momentum is transferred by the added drag (to, e.g., a turbine blade), the winds slow. Second, this change in mean-flow wind speed will create horizontal and vertical gradients in wind speed, resulting in increased turbulent transfer of momentum. As momentum is transferred from air parcels with high wind speed to air parcels with lower speed, overall kinetic energy is reduced, with the deficit dissipated as heat.

ρ_{Area} can be related to the more familiar drag coefficient. Consider air

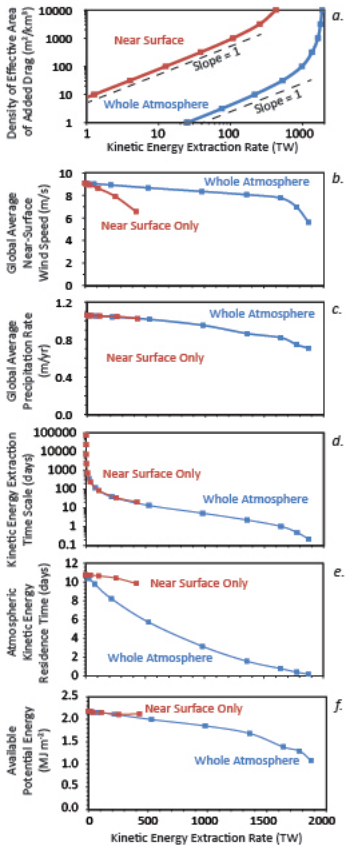

Figure A.1: Selected quantities as a function of KEE for near-surface and whole-atmosphere drag. (a) Log plot of ρ_{Area}. (b) Global average near-surface wind speed. (c) Global mean precipitation rate. (d) Kinetic energy extraction time scale. (e) Kinetic energy residence time.

with velocity $\mathbf{v}$ incident on a disk with area $\mathbf{A} = A\hat{n}$ oriented in the $\hat{n}$ direction. Let the velocity at the disk be $\mathbf{v_D}$ and the velocity in the far wake $\mathbf{v_W}$. The mass flow through the disk is therefore

$$\dot{m} = \rho \mathbf{A} \cdot \mathbf{v_D}. \tag{1}$$

Momentum is transferred to the disk by the incident air, so the disk exerts a net force

$$\mathbf{F} = m\frac{d\mathbf{v}}{dt} = \dot{m}\Delta v = -(\rho \mathbf{A} \cdot \mathbf{v_D})(\mathbf{v} - \mathbf{v_W}) \tag{2}$$

on the moving air. The rate at which the wind does work on the disk is:

$$P = -\mathbf{F} \cdot \mathbf{v_D} = \rho \mathbf{A} \cdot (\mathbf{v} - \mathbf{v_W})|\mathbf{v_D}|^2. \tag{3}$$

(Note the negative sign enters because the force is defined as the force exerted by the disk on the air, but power is defined as work done by air on the disk). Alternately, by conservation of energy, the power can be calculated as the difference between the power in the wind at the front of the disk and the power in the far wake:

$$P = \frac{1}{2}\rho \mathbf{A} \cdot \mathbf{v_D}(\mathbf{v}^2 - \mathbf{v_W}^2). \tag{4}$$

Equating (3) and (4) we find

$$\mathbf{v_D} = \frac{1}{2}(\mathbf{v} + \mathbf{v_W}). \tag{5}$$

Define $b = \frac{|\mathbf{v_W}|}{|\mathbf{v}|}$ to be the drop in wind speed across the disk. Using (5), we can now write the power as

$$P = \left[\frac{1}{2}(1+b)^2(1-b)\right] P_0 \equiv \beta P_0 \tag{6}$$

where $P_0 = \frac{1}{2}\rho|\mathbf{A}|\cos\theta \mathbf{v_D}^3$ and θ is the angle between $\hat{n}$ and $\mathbf{v}$. This is maximized at the Betz limit when $b = \frac{1}{3}$ and the power coefficient $\beta = \frac{16}{27}$.

If we define the effective kinetic energy extraction area

$$A_{eff} = \beta|\mathbf{A}|\cos\theta \tag{7}$$

the axial force becomes

$$\mathbf{F} = -\frac{A_{eff}}{(1+b)}\rho v \mathbf{v} \tag{8}$$

"Surface" drag is often defined in terms of components of the Reynolds stress tensor τ using the dimensionless drag coefficient C_D:

$$\begin{aligned} \tau_{z\rho_{Area}} &= -\rho C_D |\mathbf{v}| u \\ \tau_{z\phi} &= -\rho C_D |\mathbf{v}| v \end{aligned} \tag{9}$$

The sum of these terms yields the total force per horizontal area $A_Z = V/\Delta z$ where V is the unit atmospheric volume and Δz the vertical layer thickness. Multiplying (9) through by A_Z and equating with (8), we find that the drag coefficient is

$$C_D = \frac{A_{eff}}{V(1+b)} \Delta z = \rho_{Area} \Delta z (1+b)^{-1}. \tag{10}$$

Our parameter ρ_{Area} is therefore proportional to the drag coefficient divided by the layer thickness.

A.2 Spatial distribution of kinetic energy extraction

Figure A.2 shows the vertically integrated kinetic energy extraction rate KEE for three wind energy extraction cases. For the extreme near-surface case SL(5) ($\rho_{Area} = 10^{-5}\mathrm{m}^{-1}$ in the model's lowest two layers), 428 TW is extracted. The highest values of KEE are over ocean area and exceed 2 W m^{-2}. In the analogous whole-atmosphere case WA(7.63) ($\rho_{Area} = 10^{-7.63}\mathrm{m}^{-1}$ throughout the entire model atmosphere), 429 TW is extracted. KEE reaches maximum values exceeding 2 W m-2 between 20° and 40° latitude in both hemispheres. Finally, in the extreme whole-atmosphere case WA(5) ($\rho_{Area} = 10^{-5}$ m^{-1} throughout the entire model atmosphere), 1827 TW is extracted, with the highest values exceeding 8 W m^{-2} in a few isolated areas and exceeding 4 W m^{-2} over broad regions in the mid-latitudes. While the amount of KEE is similar in the SL(5) and WA(7.63) cases, the regions of maximum extraction in SL(5) are associated with strong mid-latitude surface winds, whereas the regions of maximum extraction in the WA(7.63) cases are associated with the jet streams. In the WA(5) case, the jets have been largely suppressed, and energy extraction is distributed over a broader geographic region.

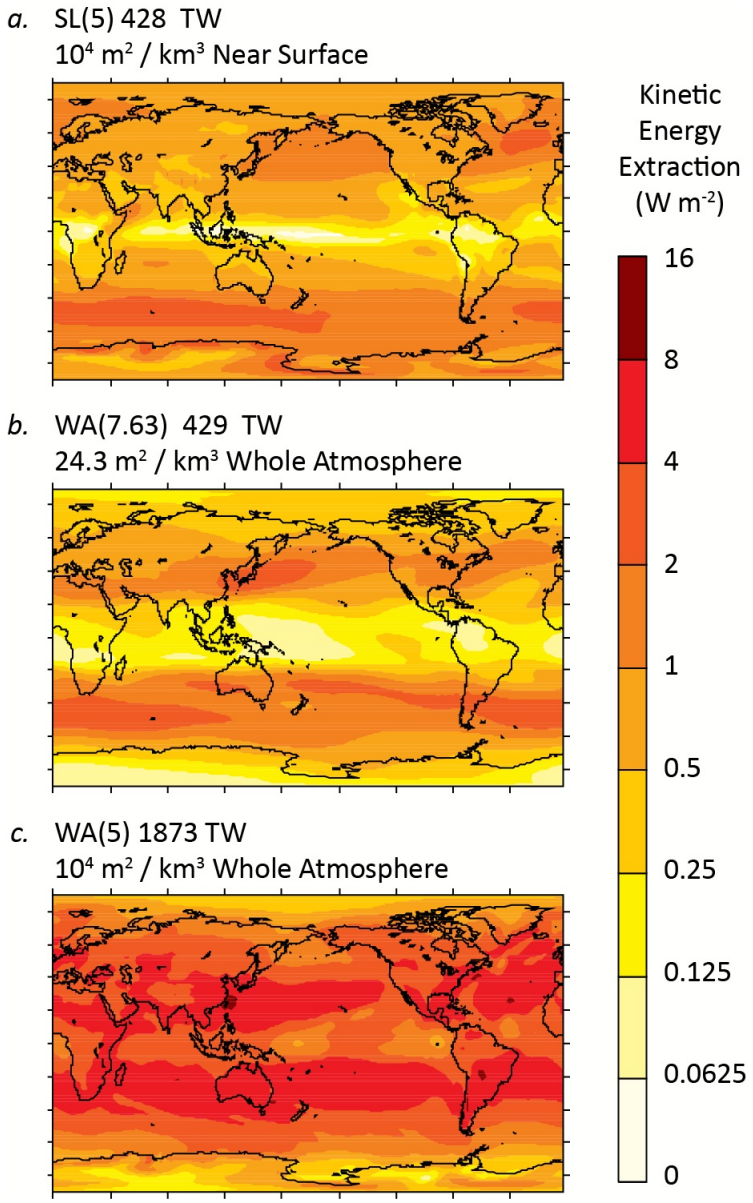

Figure A.2: Vertical integral of kinetic energy extraction (KEE) from climate model simulations with drag added near the surface and throughout the whole atmosphere: (a) SL(5), (b) WA(7.63), (c) WA(5).

A.3 Angular Momentum Constraints and the General Circulation

One major consequence of increased whole-atmosphere drag is an extension of the atmospheric Hadley regime into higher latitudes. This effect is most pronounced in the cases with the greatest amounts of added drag. In the cases with the greatest amount of added drag, there is a regime shift in atmospheric circulation characterized by Hadley cells that extend from the equator to the poles. Many global mean properties scale approximately linearly with KEE, but this scaling breaks down when the atmospheric circulation undergoes this regime shift (see Figure 1 in the main text).

The mechanisms underlying this regime shift can be illustrated by considering a ring of air above the equator that rises and begins to move poleward in an atmosphere with neither friction nor drag. Consider an azimuthally symmetric ring of air located at the equator with initial zonal velocity $u = 0$. In the absence of torques due to frictional forces or added drag, angular momentum is conserved as the ring rises and moves poleward. We therefore have

$$\frac{d}{dt}\left[ua\cos(\theta) + \Omega a^2\cos^2(\theta)\right] = 0 \tag{11}$$

where a is the radius of the Earth. As the latitude θ approaches $\pm 90°$, the zonal velocity must increase so that at latitude θ_1

$$u(\theta_1) = \Omega a \tan(\theta_1)\cos(\theta_1).$$

This expression is singular at the poles, meaning that on a rotating sphere an axisymmetric ring of air moving poleward must acquire infinite angular momentum. In practice, the development of baroclinic eddies in the mid-latitudes breaks axial symmetry, leading to the development of a pressure gradient torque which appears on the right-hand side of Eq. 11 and constrains the increase of atmospheric angular momentum.

The drag force acts opposite to the prevailing wind direction with a magnitude given by (2). This means that the conservation equation is modified:

$$\frac{d}{dt}\left[ua\cos(\theta) + \Omega a^2\cos^2(\theta)\right] = \left(-\rho_{Area}\frac{|\mathbf{v}|u}{(1+b)} + F_{\rho_{Area}}\right)a\cos\theta \tag{12}$$

where $F_{\rho_{Area}}$ is the contribution from frictional and pressure forces. If we neglect this final term, an increase in zonal velocity u also leads to an increase

in angular momentum loss due to added drag. In extreme cases, this means that the change in angular momentum of an axisymmetric ring may be very large, and the conditions that force the breaking of this symmetry may not appear; that is, direct meridional transport may become possible.

To illustrate this shift in the atmospheric circulation, we consider the meridional transport of sensible heat and momentum in the four cases discussed in the main text: the control, SL(5), WA(7.63), and WA(5). Figures A.3 and A.4 show the meridional transport of sensible heat and momentum, respectively. Figure X shows the sensible heat and momentum transport separated into mean flow and eddy contributions. In the extreme WA(5) case, eddy transport is suppressed nearly completely.

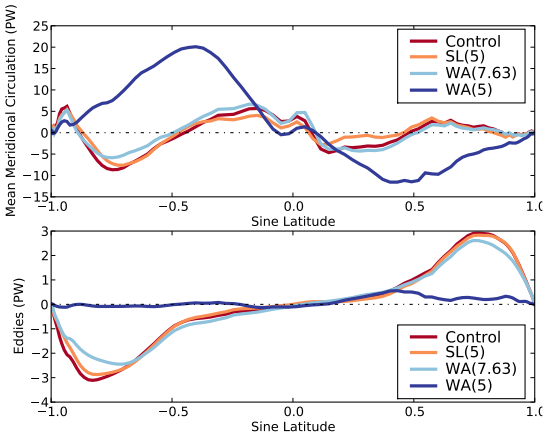

Figure A.3: Zonally and vertically averaged mean meridional (top) and transient plus stationary eddy (bottom) contributions to the meridional transport of sensible heat, in PW.

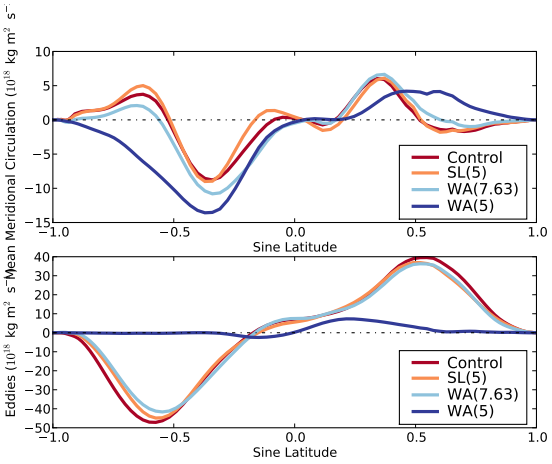

Figure A.4: Zonally and vertically averaged mean meridional (top) and transient plus stationary eddy (bottom) contributions to the meridional transport of momentum, in 10^{18} kg m^{2}s^{-1}.

Rotating annulus experiments [1] confirm that the transition to eddy-dominated regimes in an idealized case is governed by the relative strength of the Coriolis forces relative to fluid viscosity. Subsequent numerical experiments [2, 3, 4] have been performed to investigate the influence of the rotation rate on the general circulation. These studies have shown that a change in the primary mode of meridional heat transport is associated with changes in

tropospheric jet velocities and the efficiency with which the atmospheric heat engine converts absorbed solar radiation to kinetic energy. They indicate that decreasing the Earth's rotation period can lead to the disappearance of the mid-latitude Ferrel cell associated with baroclinic eddy activity, and in fact the results shown in Figures A.3 and A.4 are similar to those obtained by [3]. In experiments where there is substantial baroclinic activity, the rate of kinetic energy production is found to increase with decreased rotation rate due to the increasingly organized flow. Farrell [5] discusses a case in which an increase in the scale height of atmospheric circulation can bring about a single cell circulation leading to a decreased equator-to-pole temperature gradient. This temperature gradient reduction also occurs in experiments in which the Earth's rotation rate is slowed [3]. Our experiment differs from these studies in that we have neither increased the viscosity of the atmosphere nor altered the Earth's rotation rate, but incorporated additional momentum sinks into the whole atmosphere. However, an understanding of the behavior of the slowly rotating or viscous atmosphere can provide insight into our results. .

A.4 Energetics

The atmospheric kinetic energy cycle can be simply represented by
$G \rightarrow \boxed{\mathrm{A}} \rightarrow C \rightarrow \boxed{\mathrm{K}} \rightarrow D$
where G is the net generation rate of available potential energy, A the available potential energy reservoir, C the conversion rate between available potential and kinetic energy, and D the dissipation rate. Because we our analyzed simulation period of 60 years is long relative to the residence time of kinetic energy in the atmosphere (see Figure A1(e)), we can make the assumption that the atmosphere is in steady state, and thus $G = C = D$.

Figure 1b in the main text shows how the kinetic energy reservoir $\boxed{\mathrm{K}}$ changes with increasing kinetic energy extraction. In order to calculate how the reservoir $\boxed{\mathrm{A}}$ is affected by kinetic energy extraction, we use the approximation [6]

$$\bar{A} = \frac{1}{2} \int_0^{p_0} \frac{1}{\overline{T}} \frac{\overline{\mathrm{var(T)}}}{(\Gamma_d - \Gamma)} \, dp$$

where Γ_d is the dry adiabatic lapse rate, Γ the lapse rate, the temperature variance is calculated on pressure surfaces, and other notation is standard. This quantity is shown in Figure A1(f).

Evidently, large-scale kinetic energy extraction from the entire atmo-

sphere depletes the reservoirs of available potential energy and kinetic energy. Kinetic energy is reduced because added drag slows global average wind speeds, whereas available potential energy is reduced in large part because the temperature gradient becomes weaker, reducing the temperature variance on constant-pressure surfaces. Figure A.5 shows this variance as a function of model level for both the near-surface and whole atmosphere runs.

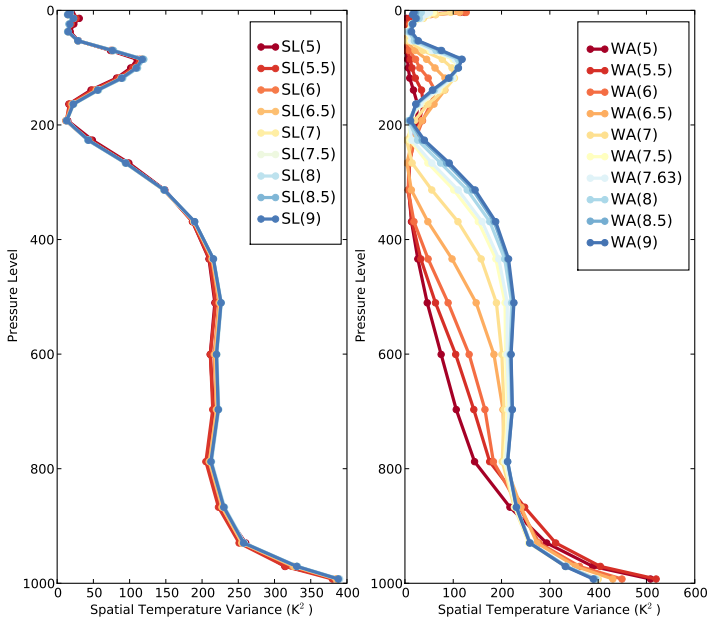

Figure A.5: Spatial variance of temperature on constant pressure surfaces as a function of height for near-surface model runs (left) and whole-atmosphere runs (right). The units are Kelvin squared.

While we assume the rate of conversion C is equal to the rate of dissipation D when integrated over the whole atmosphere, locally there may be a very large imbalance between these terms. For example, in the control case, there are large vertical motions in the mid-troposphere but most kinetic energy is dissipated at the surface or in the jet streams. We therefore consider the mechanical work done by a pressure layer on the atmosphere above it; this is the product of the pressure vertical velocity and the geopotential divided by

the gravitational acceleration. A positive(negative) work term at a constant-pressure layer indicates work done by(on) the layer on(by) the layers above. Figure A.6 shows this work term as a function of height for the control case and for SL5, WA7.63, and WA5.

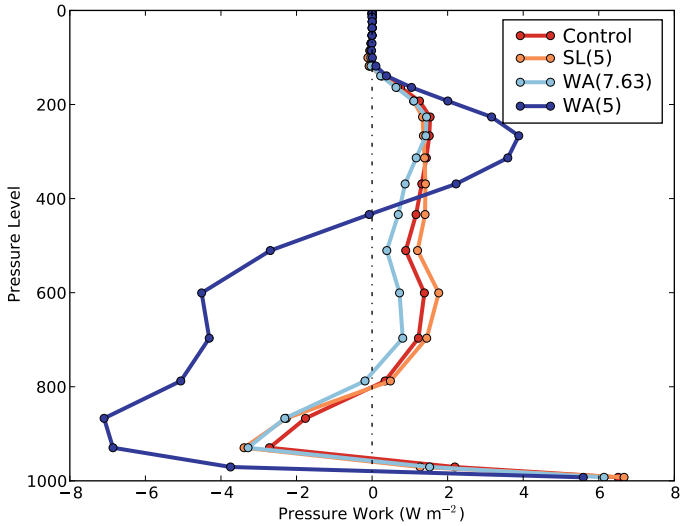

Figure A.6: Rate of pressure work done by each pressure level on the atmosphere above.

In the extreme SL(5) case, the work term becomes more negative at thse planetary boundary layer, indicating an increase in the rate of export of energy from the troposphere to the planetary boundary layer. The term becomes more positive in the mid-troposphere, indicating that the rate at which work is done by the troposphere on the stratosphere is increasing. In the WA(7.63) case, which has an amount of kinetic energy extraction similar to the SL(5) case but extracted throughout the whole atmosphere, there is likewise an increase in the downward export of energy into the boundary layer. There is also a smaller increase in the rate of upward export of energy into the stratosphere. In the extreme WA(5) case, in which direct poleward transport is the dominant transfer mechanism, we see large increases in both the downward transfer rate into the planetary boundary layer and the rate of upward transfer into the stratosphere relative to the control.

A.5 Further notes on temperature and precipitation

Introducing near-surface drag tends to increase vertical transport, enhancing turbulent transfer of heat away from the surface, an effect observed in the field [7]. However, drag forces also reduce wind speeds, tending to suppress turbulent transport. Increased vertical transport will act to cool the surface, while a reduction in wind speeds will lead to a warming effect. Figure A1(b) shows that near-surface wind speeds drop more sharply for the SL cases than for the WA cases- an unsurprising result, since the kinetic energy extraction in the SL cases takes place only near the surface. This means that the the reduction in near-surface wind speeds dominates for near-surface extraction and we therefore expect warming, while for whole-atmosphere extraction the enhanced turbulent transport is likely responsible for the surface cooling.

Ref 6 in the main text shows a nighttime temperature increase associated with high concentrations of surface-based wind turbines. Our study pertains not to high concentrations of wind turbines, but rather to uniformly distributed wind turbines. We find little cause for concern from the climate impacts of broadly distributed wind turbines at scales that could conceivably be implemented this century. However, there is a potential regional climate concern from high local or regional densities of wind turbines.

A previous study [8] considers wind power over unglaciated land only. Their measured dissipation changes by approximately a factor of two when they change model resolution, so their results may be considered an order-of-magnitude estimate. They show about 58 TW of kinetic energy dissipation over land in their most extreme case. This compares with 90 TW dissipated over land in our most extreme near-surface wind turbine case; results from all cases are summarized in Table A1 in the supplementary material.

It is useful to separate total precipitation into large-scale and convective components, and to examine the variation of these zonally averaged quantities with latitude, as in Figure A.7. Panel (a) in Figure A7 represents zonally averaged convective as a function of latitude for four cases. In the extreme surface-only case SL(5), convective precipitation decreases slightly in the Northern Hemisphere and increases slightly in the Southern. This result is consistent with precipitation changes reported by Wang and Prinn [9], who observed a shift in the location of the Hadley circulation as a result of large-scale near-surface wind extraction. The whole-atmosphere case with equivalent kinetic energy extraction, WA(7.63), appears more similar to the control, but convective precipitation is suppressed in the Southern

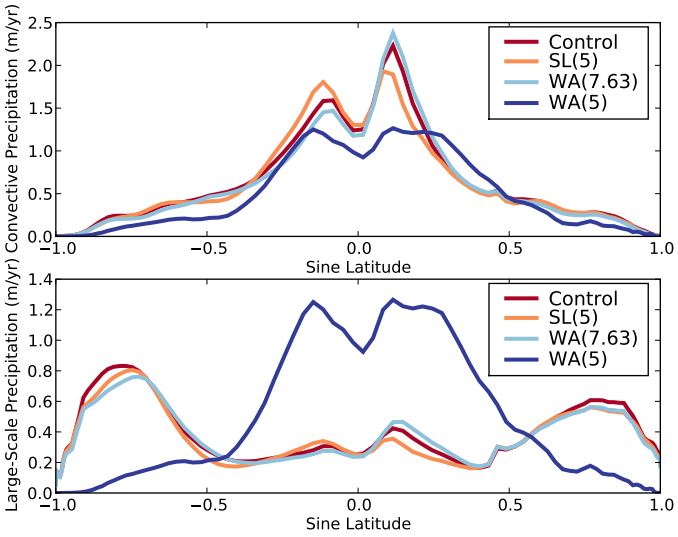

Figure A.7: Zonally averaged convective and large-scale precipitation for selected surface-only and whole-atmosphere cases.

Hemisphere and enhanced in the Northern. The extreme whole-atmosphere case WA(5)shows reduction in precipitation throughout the tropics.

Panel (b) in Figure A.7 shows zonally averaged large-scale precipitation as a function of latitude. The figure shows a decrease in mid-latitude large-scale precipitation and an increase in tropical large-scale precipitation in the WA(5) case, indicating that the mid-latitude weather systems are extremely affected by whole-atmosphere drag. The large reduction in large-scale precipitation observed in Figure A.7 is likely due to the weakening and eventual suppression of baroclinic eddy transport.

References

[1] Hide, R. An experimental study of thermal convection in a rotating liquid. *Philosophical Transactions of the Royal Society of London. Series A, Mathematical and Physical Sciences* **250**(983), 441–478 (1958).

[2] Del Genio, A. and Suozzo, R. A comparative study of rapidly and slowly rotating dynamical regimes in a terrestrial general circulation model.

Journal of Atmospheric Sciences **44**, 973–986 (1987).

[3] Navarra, A. and Boccaletti, G. Numerical general circulation experiments of sensitivity to earth rotation rate. *Climate dynamics* **19**(5), 467–483 (2002).

[4] Hunt, B. The influence of the earth's rotation rate on the general circulation of the atmosphere. *Journal of Atmospheric Sciences* **36**, 1392–1408 (1979).

[5] Farrell, B. Equable climate dynamics *Journal of Atmospheric Sciences* **47**, 2986 (1990).

[6] Peixoto, J. and Oort, A. *Physics of Climate.* American Institute of PhysicsNew York (1992).

[7] Roy, S. and Traiteur, J. Impacts of wind farms on surface air temperatures. *Proceedings of the National Academy of Sciences* **107**(42), 17899–17904 (2010).

[8] Miller, L. M., Gans, F., and Kleidon, A. Estimating maximum global land surface wind power extractability and associated climatic consequences *Earth System Dynamics* **2**(1), 1-12 (2011).

[9] Wang, C. and Prinn, R. Potential climatic impacts and reliability of very large-scale wind farms. *Atmos. Chem. Phys* **10**, 2053–2061 (2010).

List of Figures